Raghuram, G., et al., 2023, Asymmetry and evolution of craton-influenced rifted margins: Geology, https://doi.org/10.1130/G51370.1

Supplemental Material

Additional information on the geological setting of the central South Atlantic, details of numerical model, and model setup.

Movie S1.

Movie S2.

Asymmetry and evolution of craton influenced rifted margins

G. Raghuram, M. Pérez-Gussinyé, M. Andrés-Martínez, J. García-Pintado, M. Neto Araujo and J. P. Morgan

This PDF file includes:

Additional Supporting Information (Files uploaded separately)

Captions for Supplementary Movie S1, Supplementary Movie S2

S1: Maps and Distances along Flowlines

Margin Width

In this study, we relate the asymmetry of conjugate margins in the presence of a craton by comparing the margin width with the proximity of the rift to craton at rift initiation. In the central South Atlantic, from the Camamu-Gabon to the North Santos - South Kwanza margins (Fig. 1A), the extension was perpendicular to the margin (Davison, 1997; Meisling et al., 2001). We use observations for central South Atlantic by Heine et al. (2013), compiled from seismic, potential field and map data. From this dataset, we extracted: (a) the rigid crust extent which stands for areas of the crust that have not been deformed by the South Atlantic rifting, and the edges defined as landward edge of the margin (LEM), and (b) the landward limit of the oceanic crust (LaLOC). The width of the margins is the distance from LaLOC to LEM, and distance to cratons is the distance from LEM to the edge of the cratons, measured along the flowlines of the paleo reconstruction model by Pérez-Díaz and Eagles (2014) (Fig. 1A,B). In numerical models, the margin width corresponds to the length of the thinned crust i.e., the distance from the necking zone to the onset of oceanic crust measured after continental breakup, while the distance to the craton is the distance between the weak seed and the edge of the craton. Note that the margin widths do not change after break-up.

Distance to Craton

Cratons are the ancient core of the continents, with thick, cold and mechanically strong lithosphere roots. To understand the craton extent, surface geological studies assume that the

lithospheric roots are coupled to the overlying crust and describe the evolution of the cratonic blocks alongside other continental crustal tracts that form during the tectonic cycles of continental extension and collisional processes. These geological interpretations provide good first estimate of the extent of craton area during different time periods of evolution of continental blocks.

In this study, we extracted the craton boundary inferred from previous geological reconstructions. The extent of the São Francisco, Angola and Congo craton and adjacent Pan African orogenic belts at Gondwana breakup time, were obtained from Trompette and Carozzi (1994), Pankhurst et al. (2008), Van Schmus et al. (2008) and Alkmim and Martins-Neto (2012). The craton boundary configuration shown at the time of continental break-up (Fig. 1A) has also been extensively used in plate reconstructions (Aslanian and Moulin, 2013; Eagles, 2007; Heine et al., 2013). Based on these studies, the Camamu-South Gabon Margin developed with the Brazilian side close to the São Francisco Craton and the African counterpart close to the West Congo Belt. According to a more recent study (Cavalcante et al., 2019), the West Congo Belt extended northward at the location of the South Gabon basin, forming the Gabon Corridor and also that the São Francisco and Congo cratons may be connected to the north of the Camamu-South Gabon Margin.

The present-day thick lithospheric craton extent is best represented by tomographic and thermochemical studies (e.g. Afonso et al. (2022); Begg et al. (2009); Celli et al. (2020); Ciardelli et al. (2022); Feng et al. (2007)), with the caveat of poor resolution due to the paucity of seismic stations in the western African side, in particular. These results show that the surface mapped Angola craton is not underlain by thick lithosphere (Afonso et al., 2022; Celli et al., 2020). However, the existence of kimberlites in the Angolan Shield with age ranging from 124-135 Ma indicate the presence of a thick cratonic root at the time of rifting (Afonso et al., 2022; Celli et al.,

2020) , as shown in Fig. 1A. Also, some extent of the Congo craton appears to have been eroded. In South America, however, cratonic blocks appear to have been preserved (see Ciardelli et al. (2022)), indicating that the São Francisco craton lies very close to the coast line, where the rifted margin is narrow.

The distance to the craton along the South Atlantic margins shown in Fig. 1B reflects the distance from the location of extension to the craton edge at the time of break-up and corresponds to the distance from the landward edge of the margin (LEM) to the craton boundary shown in Fig. 1A.

Interpretation of Seismic Lines

The location of the interpreted seismic lines along the Camamu- South Gabon transect are shown as black thick lines in Fig. 1A. In this study, we use the previous interpretation of the seismic lines (Ros et al., 2017) shown in Fig. 1D to provide a simplified view of the conjugated margin asymmetry in terms of margin widths along with the crustal thinning profile and the faulting patterns on both the margins. The interpretation of seismic lines shows the narrow Camamu conjugate margin (~100-150 km) with abrupt crustal tapering and predominantly oceanward dipping faults while the much wider South Gabon conjugate is hyper extended (~200-250 km) with smoother crustal tapering. The seismic interpretation also indicates the asymmetric nature of the rifted margin architecture developed during a continuous rifting phase (e.g. Ranero and Pérez-Gussinyé (2010)), and not due to several rifting phases, as observed in some North Atlantic margins (e.g., Naliboff and Buiter (2015)).

S2: Numerical model formulation

For the numerical experiments, we use a 2D finite element visco-elasto-plastic code

branched from MILAMIN mechanical and temperature solvers (Dabrowski et al., 2008), and updated to include temperature and strain rate dependent non-Newtonian rheologies (see section S3 Model Rheology**),** serpentinization and melting formulations (Ros et al., 2017), stress-free top surface (Andrés-Martínez et al., 2015), plastic and viscous strain softening (see section S4 Strain Softening mechanisms), Winkler bottom boundary, surface processes coupled to the tectonics (Andrés-Martínez et al., 2019; Pérez-Gussinyé et al., 2020). Hydrothermal cooling is implemented as a parameterized solution to simulate the permeability increase along high strain-rate zones (e.g., faults) that provides pathways for the downward water circulation (see section S7 Hydrothermal cooling).

Numerical models similar to the mobile-belt models in this study are previously used to study the effect of lower crustal rheology on the melting and serpentinization (Ros et al., 2017), how surface processes coupled with rifting affects the margin architecture (Andrés-Martínez et al., 2019) and to explain the sedimentary unconformities observed at these margins (Pérez-Gussinyé et al., 2020).

The continuity equations of mass, momentum and energy are solved for incompressible Stokes flow. Velocity and Pressure are obtained by solving the Stokes force-balance equation.

$$\nabla.\tau - \nabla P + \rho g = 0$$

where τ is the deviatoric stress, P is the total pressure, ρ is the density, g the gravitational acceleration. The mass continuity equation is

$$\nabla . v = 0$$

where v is the velocity. The temperature is solved by solving the heat conservation equation

$$\rho\, C_p.\frac{DT}{Dt} = \nabla.(k\nabla T) + H_0 + H_s$$

where C_p is the effective heat capacity, T is the temperature, t is the time, k is the thermal conductivity, H_0 the crustal radioactive heat production and H_s the shear heating factor. Further details about the model setup are provided in Andrés-Martínez et al. (2019) and Pérez-Gussinyé et al. (2020).

The surface processes in the numerical model is similar to that in Andrés-Martínez et al. (2019) and Pérez-Gussinyé et al. (2020). The landscape evolution in the sub-aerial domain is modelled using 1-D sediment mass conservation equation combining the hillslope and the fluvial transport processes as

$$\frac{\partial h}{\partial t} = \frac{\partial}{\partial x}\left((K + cq_w^n)\frac{\partial h}{\partial x}\right)$$

where K is the slope diffusivity, c is the transport coefficient, q_w is the water flux and $n \geq 1$ is the power law relating the sediment transport with the water flux.

By assuming a constant water discharge/rainfall δ, the water flux at downstream locations over the surface can be described as

$$q_w = \delta x_d$$

where $x_d$is the integrated downstream distance from topographic highs to the valley bottom, calculated at each timestep.

In the submarine domain, the relationship between the sediment transport and the water flux is given by

$$\frac{\partial h}{\partial t} = \frac{\partial}{\partial x}\left(K_s e^{(-\lambda_s h_w)}\frac{\partial h}{\partial x}\right) + S$$

where K_s is the submarine diffusion coefficient, λ_s is the submarine diffusion decay coefficient

and h_w is the water depth and S is the hemipelagic sediment rate. The sea-level is calculated isostatically at the start of the model assuming, sea-level is at 0 km depth for a crust of 30 km.

We calculate the tectonic subsidence in the models with surface processes, by unloading the sediments using variable flexural rigidity along the thinned margins. At each time step, the flexural rigidity is calculated from the strength profile using the formulation by Burov and Diament (1995).The flexural rigidity along with the sediment thickness at the margins provide an estimate of the flexural rebound of the basement during the sediment unloading or backstripping process (e.g., Cunha (2008)). This flexural rebound is used to calculate the tectonic subsidence on the conjugate margins at each timestep. The calculated backstripped basement depths through the model evolution, for the locations shown by markers on either margin are shown in Fig. 4C and Movies S1, S2.

S3: Model Rheology

The constitutive equation between the deviatoric stress (τ), in Stokes force-balance equation and the deviatoric strain rate ($\dot{\varepsilon}'$) is given by

$$\tau = \eta_{eff} \left(2\dot{\varepsilon}' + \frac{\tau^{oldJ}}{\mu \Delta t}\right)$$

where η_{eff} is the effective viscosity, τ^{oldJ} is the Jaumann corotational stress, μ is the shear modulus and Δt is the numerical time step. The effective viscosity formulation depends on whether the material yields plastically or undergoes visco-elastic deformation. Following the Drucker-Prager yield criterion, plastic deformation in the material dominates when the second invariant of the deviatoric stress τ_{II} is larger than or equal to the plastic yield stress σ_y, which is defined as

$$\sigma_y = P \sin \varphi + C \cos \varphi$$

where P is the pressure, φ and C are the friction angle and cohesion of the rock respectively.

The plasticity formulation can be included in the viscous formulation by the Prandtl–Reuss flow law (similar to that in Andrés-Martínez et al. (2019)) for yielding materials when $\tau_{II} = \sigma_y$, by defining the effective viscosity η_{eff} as

$$\eta_{eff} = \frac{\sigma_y}{\left(2\dot{\varepsilon}' + \frac{\tau^{oldJ}}{\mu\Delta t}\right)_{II}}$$

where $()_{II}$ is the square root of the second invariant operator (Moresi et al., 2003). But when $\tau_{II} < \sigma_y$, the material deforms visco-elastically, and the effective viscosity η_{eff} is given by

$$\eta_{eff} = \left(\frac{1}{\eta_{dis}} + \frac{1}{\eta_{dif}} + \frac{1}{\mu\,\Delta t}\right)^{-1}$$

where η_{dis} and η_{dif} are the dislocation and diffusion creep viscosities respectively.

The viscous creep flow is defined by the non-linear power law dependent temperature and stress-dependent rheologies as:

$$\eta_{dis/dif} = \mathrm{S}\,(\gamma \mathrm{B})^{-\frac{1}{n}} \dot{\varepsilon}_{II}^{\frac{1-n}{n}} exp\left(\frac{E + PV}{nRT}\right)$$

where S is scaling parameter obtained from uniaxial/triaxial experiments (for principal stresses) to second-invariant-strain rate formulation of the viscosity, γ is a weakening factor (see section S4: Strain Softening), B is the pre-exponential factor of the flow law, n is the power-law exponent, *E* is the activation energy, *V* is the activation volume, *R* is the gas constant, and *T* is the absolute temperature. The values of these parameters are given in Table S1.

The numerical model domain is composed of: (1) a wet quartzite upper crust (Gleason and Tullis, 1995), (2) a wet anorthosite lower crust (Rybacki and Dresen, 2000), (3) dry olivine lithospheric mantle (Hirth and Kohlstedf, 2003), and (4) wet olivine asthenosphere (Hirth and

Kohlstedf, 2003).The wet anorthosite rheology is chosen for the lower crust, as a representative of intermediate strength profile between the strong mafic granulite and the weak wet quartzite rheologies (e.g. Andrés-Martínez et al. (2019); Pérez-Gussinyé et al. (2020)). In the numerical model, the viscosity of the materials is limited between the values from 10^{18} Pa.s to 10^{24} Pa.s.

During the model run, melting is self-consistently calculated following the formulation given by Ros et al. (2017), so that as the lithosphere extends and mantle upwelling occurs, decompression melting occurs when the mantle temperature exceeds the solidus.

The melting in the mantle depletes the mantle source and decreases the mantle density. From the reference densities used for different layers (Table S1), the density changes with temperature and also the amount of depletion. The density in the model follows the Boussinesq approximation (Ranalli, 1995), and is expressed as $\rho = \rho_0(1 - \alpha(T - T_0) - \beta F)$, where ρ is the density, α is the thermal expansivity, β is a factor that parameterizes the influence of melt extraction on density and is equal to 0.044 (Armitage et al., 2014), F is the melt depletion, ρ_0 is the reference density and T_0 is the reference temperature, 0° C.

The initial melt depletion profile along with temperature also influences the composition of the lithospheric mantle and asthenosphere. The lithospheric mantle is modelled as dry olivine with 4% constant melt depletion. Asthenospheric mantle is modelled as wet olivine with water content of 500 ppm H/Si and 0% initial depletion. The effect of depletion on the viscosity is dependent on the amount of water in the asthenospheric mantle and results in viscosity increase with increasing dehydration during the melting phase. To simulate this effect of increase in viscosity during melting in the asthenospheric mantle, i.e., as the melt depletion increases from 0% to 4%, the rheology is modelled as a mixture of wet and dry olivine with increasing proportion of dry olivine. Thus, in asthenospheric mantle, for melt depletion greater than or equal to 4%, all

the water is assumed to be extracted from the melt residue (Morgan, 1997) and rheology changes from wet to dry olivine. Further, at the lithosphere-asthenosphere boundary (LAB), melt depletion is linearly reduced from 4% to 0% representing a smooth, 5 km wide, transition for the dry-wet olivine interface (Fullea et al., 2011; Khoza et al., 2013).

S4. Strain softening mechanisms

Faults and shear zones form in the plastic and viscous domain when deformation localizes into these weakened bands and further weakens these zones. The effect of strain weakening in the viscous domain is implemented by the reduction in effective viscosity with increase in viscous strain during the development of shear zones. Various processes are suggested to explain the strain softening mechanisms like dynamic recrystallization causing a reduction in the grain-size (Handy et al., 2007), dissipative heating (Regenauer-Lieb et al., 2006), phase changes (Brodie and Rutter, 1987) and the development of lattice preferred orientations in the upper mantle (Tommasi et al., 2000). The dynamic recrystallization mechanism is found to play a fundamental role in rheological weakening during the development of shear zones in the viscous domain (Platt and Behr, 2011). It is also shown that the strain softening effects are limited to temperatures > 800 ºC and reduces with temperature (Précigout and Gueydan, 2009). To simulate the overall effect of rheological weakening broadly based on these studies, we introduce a factor γ in the viscous creep flow formulation used in the numerical model. This temperature-dependent factor γ decreases with an increase in the accumulated second strain invariant ϵ_{II} and is given by

$$\gamma(T) = \left(\epsilon_{IIf} - \epsilon_{II}\right) \frac{\gamma_2(T) - \gamma_1}{(\epsilon_{IIf} - \epsilon_{IIi})} + \gamma_1$$

where $\gamma_2(T)$ is temperature dependent with a value of 20 between 0ºC and 800ºC followed by an exponential decrease from $\gamma_2(T)$ = 20 at 800ºC to $\gamma_2(T)$ = 1 at 1200º C, γ_1 = 1, ϵ_{IIf} = 1 and ϵ_{IIi} = 0 for viscous strain softening factor $\gamma(T)$ ranging from 1 to 20. For a value of 20, this will

correspond to a maximum reduction of 0.42 in the effective viscosity at 800°C and decreases exponentially with increase in temperature to 1200°C (Précigout and Gueydan, 2009).

In mobile-belt model experiments, an increase in the viscous strain softening (VSS) factor γ_1, increases the degree of asymmetry in the final rifted margin architecture. In Fig. S3 (A-C), we show how a mobile-belt model with initial crustal thickness of 40 km is almost symmetric when the VSS factor $\gamma_1 = 1$ i.e., when there is no strain softening in the viscous domain in the model. But, with increasing VSS factor i.e., at T = 800ºC for $\gamma_2(T) = 10$ to $\gamma_2(T) = 20$, the asymmetry in the models increases while all the other parameters in the models remain constant.

In the plastic domain, faults represent the discontinuities along which mechanical rock strength decreases with increase in the accumulated plastic strain. In numerical models, the reduction in the yield stress with increase in plastic strain is simulated by using a linear parametric function that reduces the initial friction angle of 30º (friction coefficient of 0.577) to 15º (friction coefficient of 0.268) when the accumulated plastic strain increased from 0 to 1. Cohesion is kept constant throughout the model evolution at 10 MPa.

S5: Initial and boundary conditions for mobile belt and craton models

The initial model domain for both mobile-belt and craton models is 600 km wide and 300 km deep box and is discretized using a Lagrangian mesh composed of triangular elements, which increases in width due to the prescribed velocity boundary conditions. The mesh element resolution of 1 km in the upper crust, 2 km in the lower crust and 5 km in the mantle respectively. The rheological lithosphere-asthenosphere boundary (LAB) is at an initial depth of 110 km in the mobile-belts.

Full extension velocity (V_{ext}) is 10 mm/yr, to reproduce the initial rifting velocities in the central South Atlantic. The boundary conditions are half-extension velocities applied to the lateral

boundaries of the model box in all the numerical experiments. The model has a free surface on the top and is supported by a Winkler foundation at the bottom.

In the mobile-belt models, the temperature boundary conditions are 0ºC, 1300ºC at the top and bottom of the model, respectively. In addition, the region located between the initial LAB boundary (which is at 110 km in mobile belts) to the bottom of the model is also kept constant at 1300ºC during the model run, as it is assumed to have a negligible adiabatic gradient (0.3ºC/km, (Phipps Morgan, 2001). The rheological LAB is tracked with tracers through time, so the position of the LAB is known at every timestep. The temperature of the asthenosphere between the initial LAB depth (110 km) to the bottom of the boundary is always maintained at 1300ºC. As the rifting evolves and the lithosphere thins (to depths shallower than the initial rheological LAB depth), the whole asthenosphere-lithosphere system is allowed to conductively cool. Evidence of this cooling is observed in slow and ultra-slow spreading systems.

The setup for craton model experiments is shown in Fig S1. In nature, the observed cratonic crustal thickness varies from 35 to 50 km thickness (Durrheim and Mooney, 1994; Ford et al., 2010). The crust at cratons is inferred to be mostly felsic (Delph and Porter, 2015) with the exception of areas affected by plumes, while mobile belt is found to be slightly more mafic (Kgaswane et al., 2009). However, for simplicity, we assume that the crustal thickness and composition in the cratonic lithosphere is the same as that of the adjacent mobile belts. The cratons are simulated with a 200 km thick lithosphere and placed adjacent to the normal continental lithosphere of 110 km thick lithosphere with transition between cratonic and mobile-belt lithosphere is modelled as sharp transition that occurs at an angle of 80º ((Ritsema and van Heijst, 2000), but note that we also tested models with other slopes at the transition (Section S8). The temperature boundary conditions are 0ºC and 1300 ºC at the top and bottom of the model. Just like

in the mobile-belt models, the rheological LAB in craton models (Fig. S1) is tracked with tracers through time, so the position of the LAB is known at every timestep. Throughout the craton model experiments, the temperature of the asthenosphere is kept to 1300 ºC, in the area located between the model bottom and the tracked rheological LAB, with exception of the areas where the lithosphere has thinned enough, so that the tracked LAB is less than 110 km (i.e., the initial mobile belt LAB depth).

In the craton models, the thick craton region is simulated to have a lateral extent of 200 km (Fig. S1). In this study, we test the effect of the influence of the proximity of a craton on the polarity of conjugate margin asymmetry by initiating rifting using the thermal weak seed at 50, 100 and 200 km distances from the craton edge. Since we use a model setup with initial lateral extent of 600 km, even when the thermal weak seed is placed at 200 km from the craton edge, the right lateral boundary is still 200 km away from the rift locus. Our experiments with mobile-belt models and previous studies (Andrés-Martínez et al., 2019; Pérez-Gussinyé et al., 2020) confirm the rift evolution with lateral boundaries >= 200 km from the rift locus is essential to avoid any edge effects on the rift evolution.

S6: Initial weak seed and Randomization of the initial friction angle

In numerical modelling studies, weak seeds are used to initiate deformation at a particular choice of location. We use a 2D-Gaussian temperature weak seed of 10 x 20 km size located at 30 km depth and 100ºC maximum temperature increment, which allows the experiments to initiate rifting in regions of interest. The increase in temperature associated with thermal weak seed diminishes by thermal diffusion, in the first 4 - 5 m.y., as the model evolves (Movie S1). We also tested the model setup with a weak seed consisting of over-thickened crust of size (20 km x 4 km) at the bottom of the lower crust (Fig. S7A). The evolution of asymmetric margins in the craton

models is consistent with those from the numerical experiments using the thermal weak seed to initialize deformation in the models (Fig. S7B).

In the plasticity formulation of the numerical model, at model start, we add a random field varying between -1 to 1 multiplied by the amplitude of variation of 2^{o} to the initial friction angle at each integration point so that the initial friction angle varies in space with values between 28^{o} - 32^{o}. Note that this random field is not constrained spatially, so it doesn't imply any localized spatial heterogeneities and extends throughout the domain space (Fig. S2). This is intended to simulate the natural heterogeneities that may affect the plastic strain localization. The random initial friction angle is then reduced linearly to final friction angle of 15^{o} in the range of accumulated strain from 0 to 1.

The randomization in the initial friction angle parameter is implemented in order to analyze the polarity of the asymmetry in the numerical experiments. For each configuration of mobile-belts and craton models, we run models with 10 different randomized friction angles with all the other parameters kept constant. Note that, the 35 km thick crust mobile-belt models evolve into symmetric conjugate margins, so the randomization effect of the initial friction angle is not evident (Fig. 3B). For mobile-belt models with 40 km crustal thickness, identical models with different initial friction angle randomizations result in different polarity of the asymmetry, as shown in Fig. S3(E, F). Out of the 10 numerical experiments for mobile-belt models with 40 km crustal thickness, 6 simulations show polarity of the asymmetry on one side while the other 4 simulations show polarity of the opposite sense.

However, in craton models with the same 10 randomizations in initial friction angle as mobile-belt models, we observe that all the experiments result in similar polarity of the rift

asymmetry, i.e., the narrow margin of the asymmetry always occurs on the craton side irrespective of the initial crustal thickness used in models (35 km or 40 km).

S7: Hydrothermal Cooling

To consider the cooling effects of seawater circulation, we implement a parameterized conductive hydrothermal cooling that effects the thermal conductivity, *k,* along active faults, which are the main conduits for fluids (Morgan and Chen, 1993):

$$k = Nu \cdot k_0$$

where, k_0 is the background conductivity and Nu, is a function of a nominal plastic strain rate $\dot{\varepsilon}^H$ and a corresponding nominal Nu_{max}. The deformation-dependent function to estimate Nu is given by:

$$Nu = 1 + (Nu_{max} - 1)\left(1 - e^{\left(-\frac{3\dot{\varepsilon}_{II}^{p}}{\dot{\varepsilon}^{H}}\right)}\right)$$

where $\dot{\varepsilon}_{II}^{p}$ is the second invariant of the plastic strain-rate, which is used as a proxy for permeability. In this study, we set $Nu_{max} = 10$, and $\dot{\varepsilon}^H = 1 \times 10^{-13}$ s^{-1}. The hydrothermal cooling is active at depths where temperature is less than 600°C isotherm, the maximum temperature at which the permeability of rocks is expected to be too low for fluid flow. According to our formulation, implies that the intensity of cooling increases with increasing localization. The parameterized hydrothermal cooling favors the development of deep penetrating brittle faults during the final stages of rifting, thereby promoting break-up compared to models without hydrothermal cooling.

S8: Influence of LAB slope at the craton-mobile belt edge

In this study, the craton models are simulated by replacing the normal continental lithosphere on one side of the lateral domain by a 200 km thick lithosphere (Fig. S1). We primarily use the craton models with a steep transition of 80° to test our hypothesis and discuss the

implications on the degree and the polarity of the asymmetry of the rifted conjugate margins. However, we tested different model setups with the slope of transition between the thick cratonic lithosphere adjacent to the continental lithosphere ranging from 20^{o} - 60^{o} in steps of 20^{o}.

The results of these craton models, are consistent with those observed in models with steeper slope (80^{o}) of LAB transition (Fig. S6) in terms of the polarity and degree of rift asymmetry. We conclude that the slope of the LAB transition at the craton mobile-belt edge has no effect on the degree or polarity of the asymmetry in the final margin conjugate architecture. We also observe the cratonic lithosphere remixing with the adjacent convective asthenosphere in all the configurations of the slope of the LAB transition at the craton mobile-belt edge. The slope of the LAB at this edge however affects how this transition evolves as rift progresses in time. It is observed that at gentler slopes of transition from 20^{o} - 60^{o}, the craton mobile-belt edge doesn't get significantly weakened locally at any point along the junction. Rather, the horizontal component of the asthenospheric flow uniformly affects the entire LAB junction when the transition gently slopes towards the mobile-belt. However, at a steep angle of LAB transition (at 80^{o}), it is observed that the sharp transition results in a small undulation in the cratonic lithosphere early in the synrift phase (Fig. S4) that grows into a sub-horizontal channel driven by the asthenospheric flow (Movie S2). In models with the steep angle of the LAB (at 80^{o}) at the craton mobile-belt edge, this sub-horizontal channel is observed at the depth of around 110 km i.e., the initial depth of mobile belt LAB, and forms as a result of focused asthenospheric flow at this location.

S9: Stability of the craton

In the craton model setup, the craton lithosphere at the craton-mobile-belt interface is modelled as strong and buoyant compared to the adjacent asthenospheric mantle. Previous numerical studies indicate that a strong lithosphere is necessary for maintaining the integrity of the

lithospheric root from the adjacent mantle convection flow (Doin et al., 1997; Lenardic and Moresi, 1999; Salazar-Mora and Sacek, 2021). In the model setup, the rheology of the mantle (dry olivine for mantle lithosphere and wet olivine for asthenosphere) along with low geothermal gradient in the craton results in a strong lithospheric root adjacent to the asthenosphere at the craton mobile-belt edge. To test the stability of the lithospheric step at the craton-mobile belt edge, we run the simulations with the craton setup with full extension velocity of 0.1 mm/year (Fig. S5). We observe instability and associated flow in the asthenosphere at the craton-mobile-belt edge, because of the Winkler boundary condition at the bottom, and the lateral heterogeneity in the lithospheric thickness, but the small edge driven convection observed is in the reverse sense to that observed in the craton models with finite extension (Fig. S4). The craton-mobile belt boundary has not deformed significantly for almost 30 m.y. (Fig. S5) and the lithospheric root of the simulated craton is also not affected significantly during this time. We also find the thermal field to be in steady state and consistent with the geothermal gradients for the mobile-belt and craton lithosphere. Also note that there is no sign of the temperature perturbation used in the initial thermal weak seed (100^{o}C) in the crust (Fig. S1) which gets diminished within 3 - 4 m.y. after rift onset.

Figure S1: Model Setup

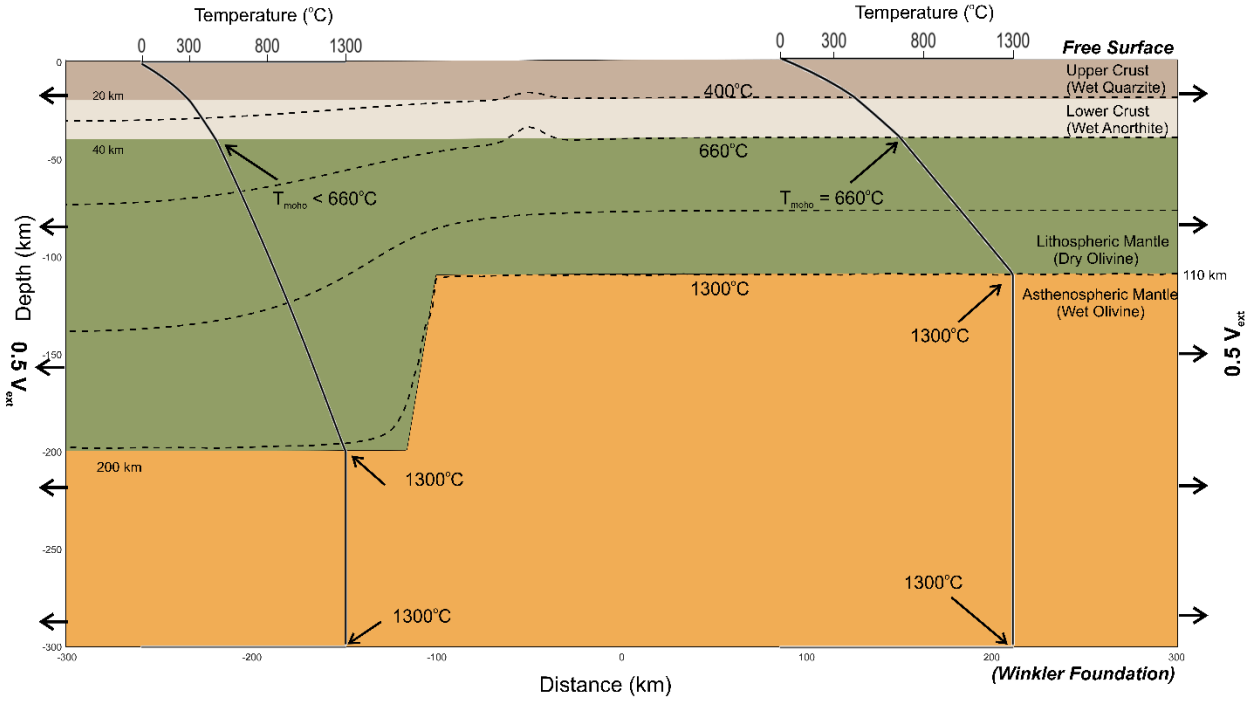

Figure S1 **Model Setup** The initial model domain extending over 600 km laterally and 300 km deep. The temperature profiles in the mobile-belt side with lithospheric thickness of 110 km and the craton side with lithospheric thickness of 200 km are shown. The thermal weak seed of 10 x 20 km size located at 30 km depth with a maximum increase in 100°C is laterally at a distance of 50 km from the craton mobile-belt edge. Half extension velocity (0.5 * V_{ext}) is applied on either side of the domain. The model has free surface on the top and supported by Winkler foundation at the bottom. Note the lower geothermal gradient of the simulated craton lithosphere compared to that of the adjacent mobile-belt lithosphere.

Figure S2: Randomization of initial friction angle

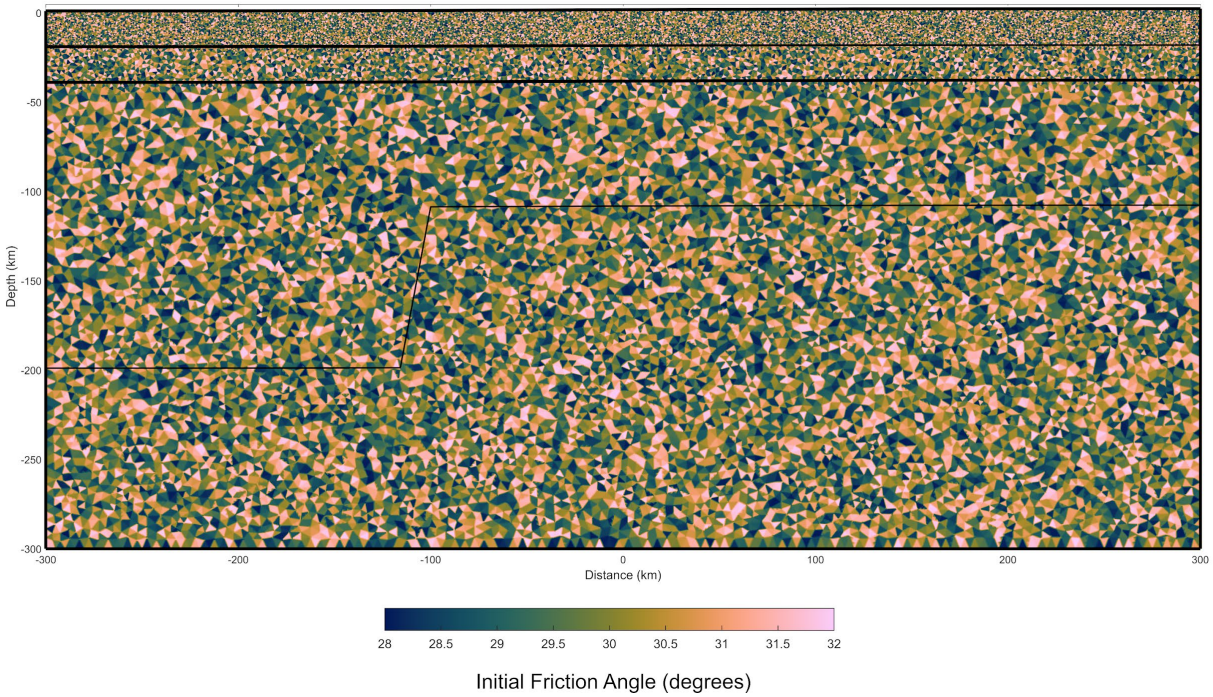

Figure S2 Plot of the randomized initial friction angle at the integration points spread throughout the model domain to simulate the natural heterogeneities observed in nature. The friction angle at model start (initial condition) is randomly varied between 28º to 32º and with increasing accumulated strain, the strain softening function linearly decreases the friction angle to 15º.

413 **Figure S3: Mobile-belt Models**

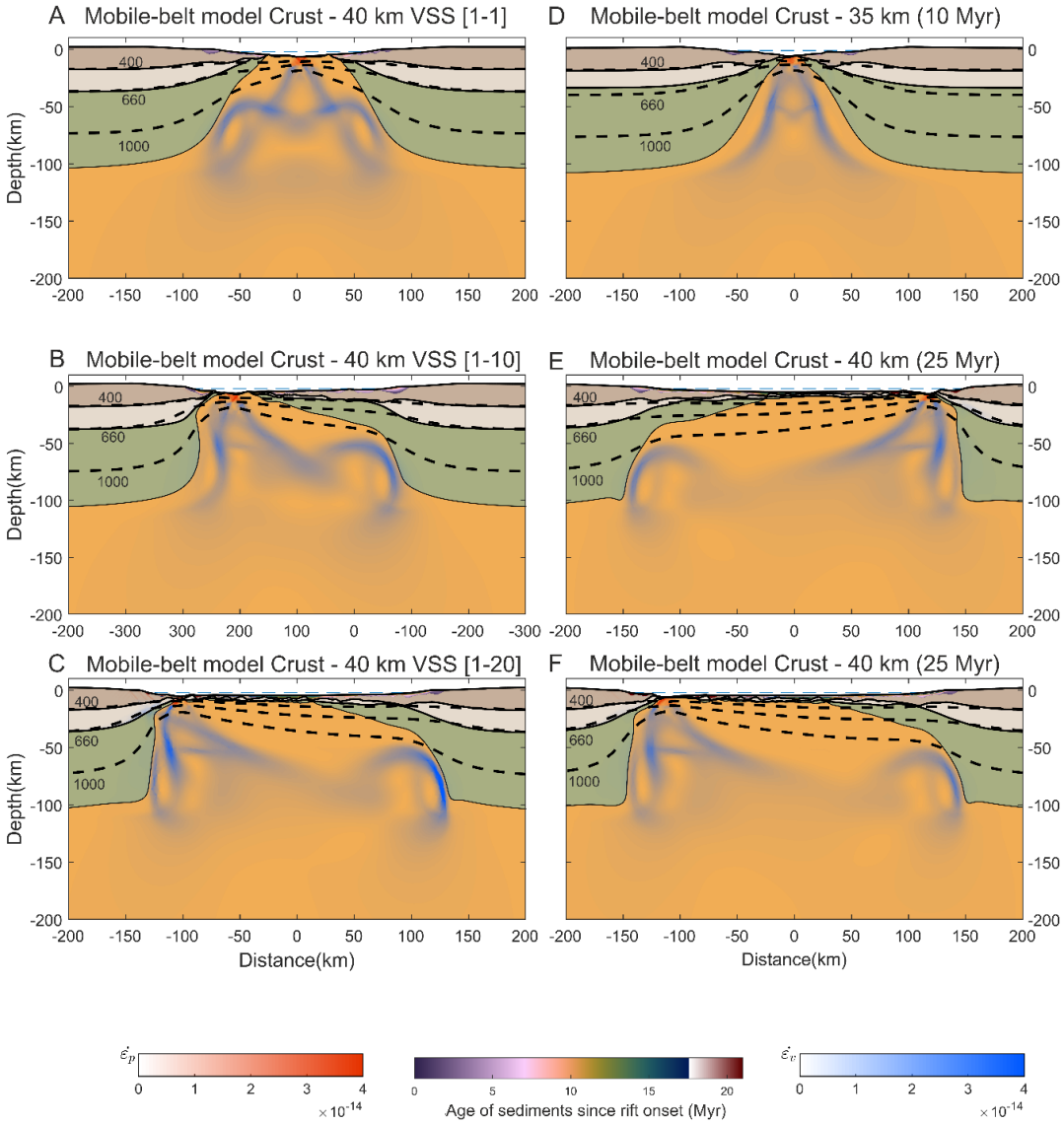

414

415 **Figure S4: Craton model Evolution**

Figure S3 Configuration for chosen time steps for different numerical experiments of mobile-belt models. Discontinuous black lines represent isotherms [^{o}C]. (A) Mobile-belt experiment with 40 km thick crust with viscous strain softening parameter (VSS) factor ranging from 1 -1 i.e., no strain softening is applied in the model, (B) and (C) are the same as (A) but with increasing VSS factors ranging from 1 to 10, and 1 to 20 and (A-C) Mobile-belt models are at the breakup time (~22 m.y.) in their evolution. Asymmetry increases with increasing maximum VSS factor. Unless specified, the VSS factor used in this study is 1 to 20. (D) Mobile-belt models with 35 km crust, results into symmetric conjugates. (E, F) Mobile-belt models with 40 km crust resulting in asymmetric margins but opposite polarity. The experiments (E, F) differ in the spatial randomization of the initial friction coefficient, which varies between 28^{o} - 32^{o}. Note that geometries and length of the margins are similar but polarity of the asymmetry is inverted. Plastic, viscous strain rates [s^{-1}] are shown in red, blue shadings respectively and sediments color-coded by age are shown.

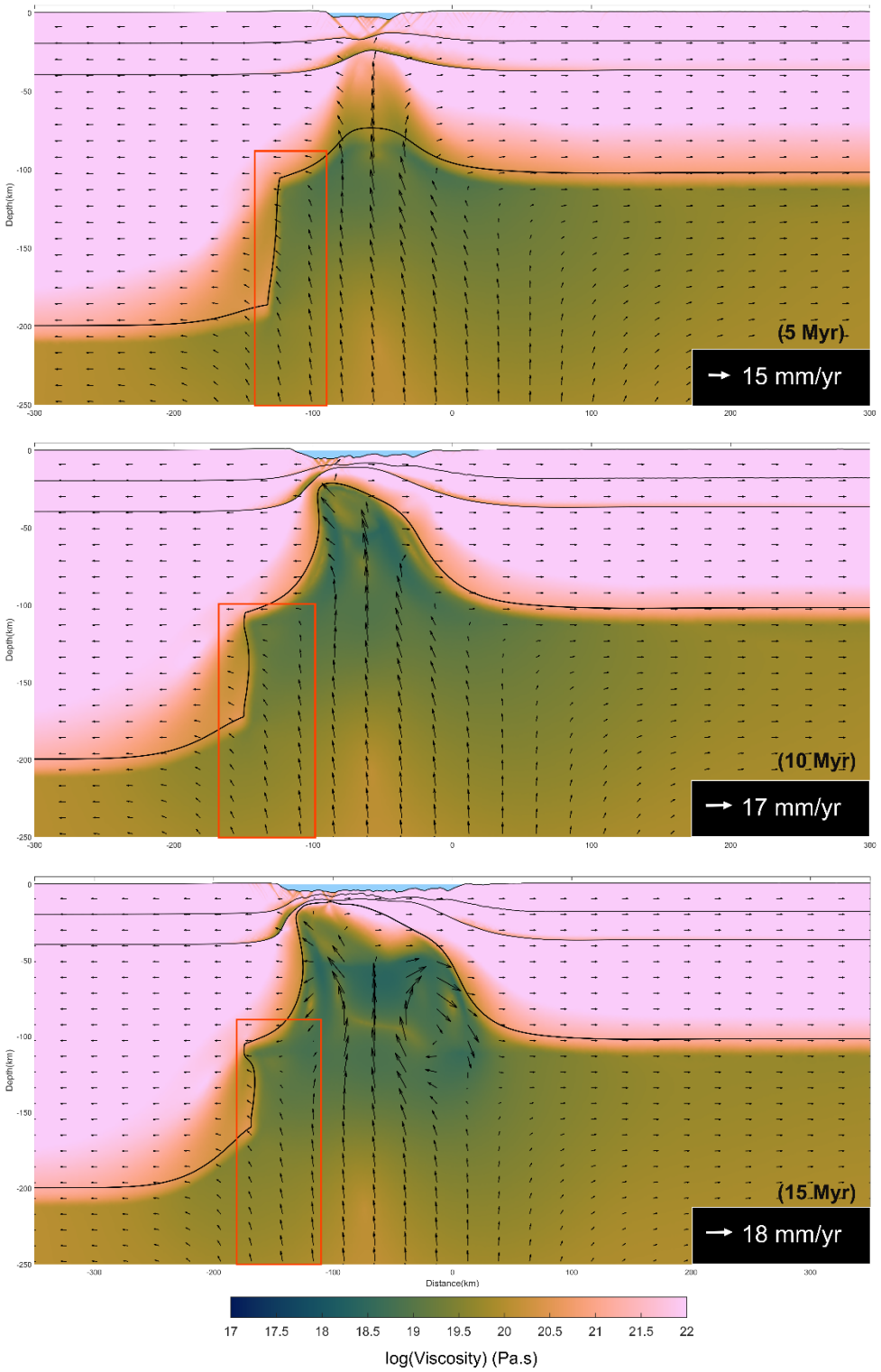
Depth(km)
(5 Myr)
15 mm/yr
(10 Myr)
17 mm/yr
(15 Myr)
18 mm/yr
Distance(km)
17 17.5 18 18.5 19 19.5 20 20.5 21 21.5 22
log(Viscosity) (Pa.s)

416

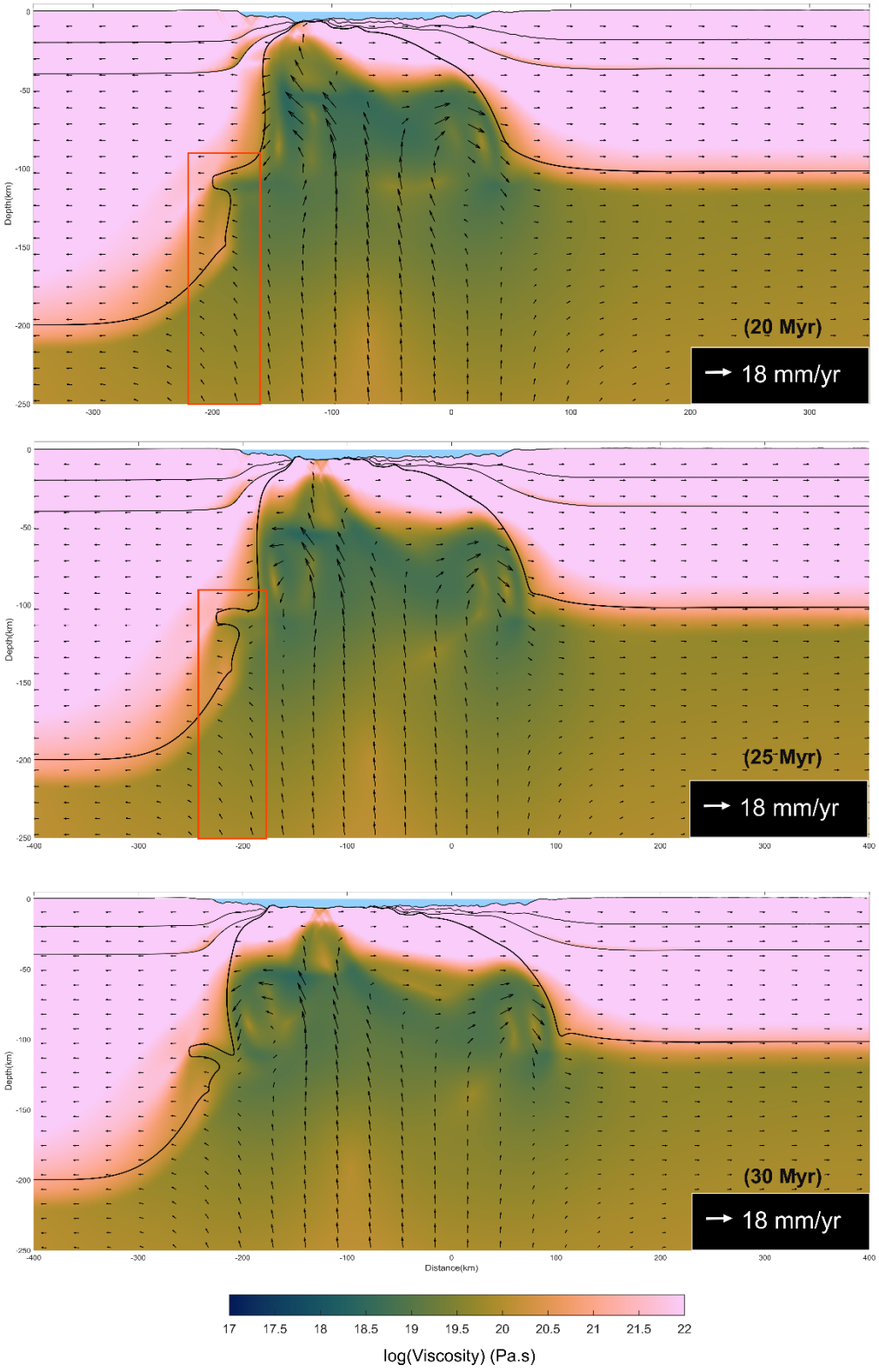
Depth(km)
(20 Myr)
18 mm/yr
(25 Myr)
18 mm/yr
(30 Myr)
18 mm/yr
Distance(km)
17 17.5 18 18.5 19 19.5 20 20.5 21 21.5 22
log(Viscosity) (Pa.s)

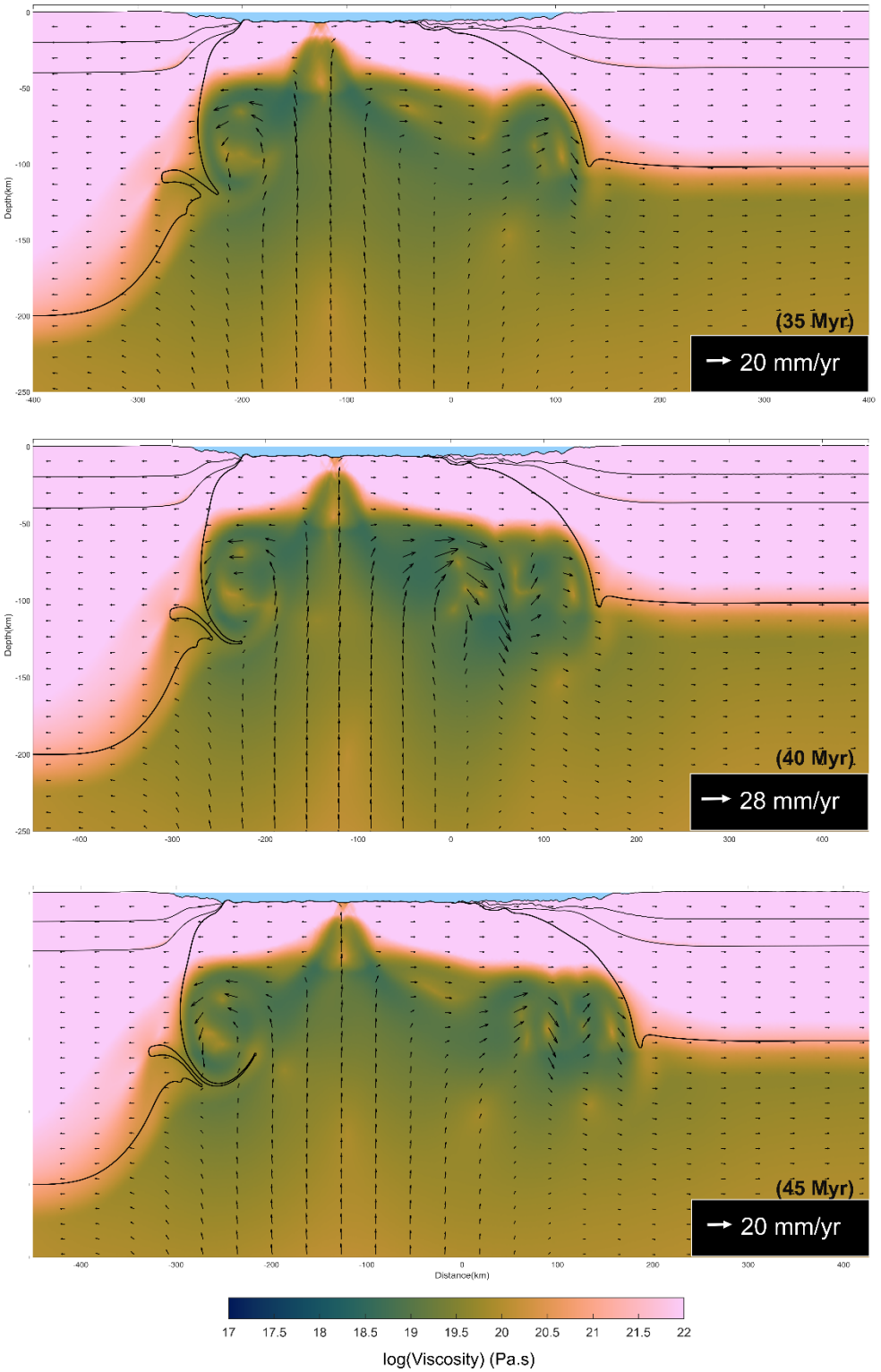

Figure S4 Snapshots of the craton model with initial crustal thickness of 40 km at different timesteps of the evolution till 45 m.y. Viscosity field is plotted showing the evolution of the geometry of the lithosphere-asthenosphere boundary (LAB) along with the velocity vectors. The LAB at the craton-mobile-belt junction

experiences high strain rates (refer to Fig. 2E). Also, note the gradient of horizontal velocity of asthenospheric flow from bottom to top observed adjacent to the craton (highlighted by the red box) that results in the deformation at the depth of 100 – 110 km (depth of the mobile-belt LAB). and forms finger like structure during the early stages of evolution of the model simulation (5 m.y.- 25 m.y.). This sub-horizontal channel in the cratonic lithosphere evolves over time, weakening this area. After 25 m.y., the shallow convection adjacent to the craton lithosphere will deform the craton lithosphere above this sub-horizontal channel and results in fragmentation (Refer to Movie S2). The sea-level and water is represented by the cyan patch on the top.

Figure S5: Craton model with negligible extension

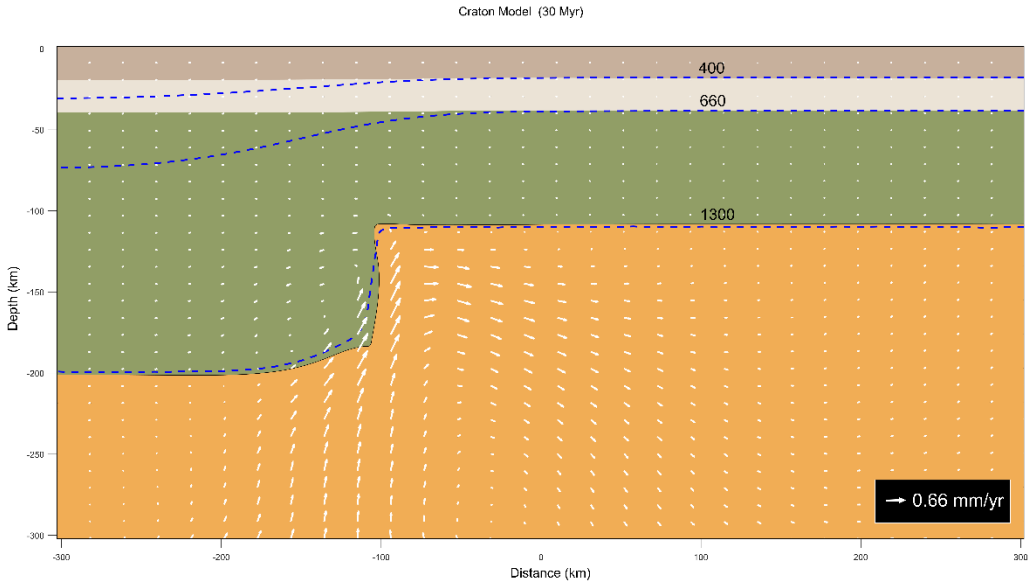

Figure S5 Snapshot of the craton model with initial crustal thickness of 40 km and thermal weak seed at 50 km from the craton edge with negligible extension (full extension velocity of 0.1 mm/yr) at the lateral boundaries at 30 m.y. The color codings for layers is similar to that of Fig. S1. The isotherms are shown in blue dashed lines with labels indicating the temperature [ºC] at the base of upper crust, lower crust and the LAB. The velocity vectors are shown in white indicating the flow of asthenosphere caused by the steep lithospheric step at the craton mobile-belt edge. The edge driven convection caused by the lithospheric step at the craton mobile-belt edge is in the opposite direction to that in craton models with finite extension on the lateral boundaries.

Figure S6: Craton Models with different slopes of craton-mobile belt edge

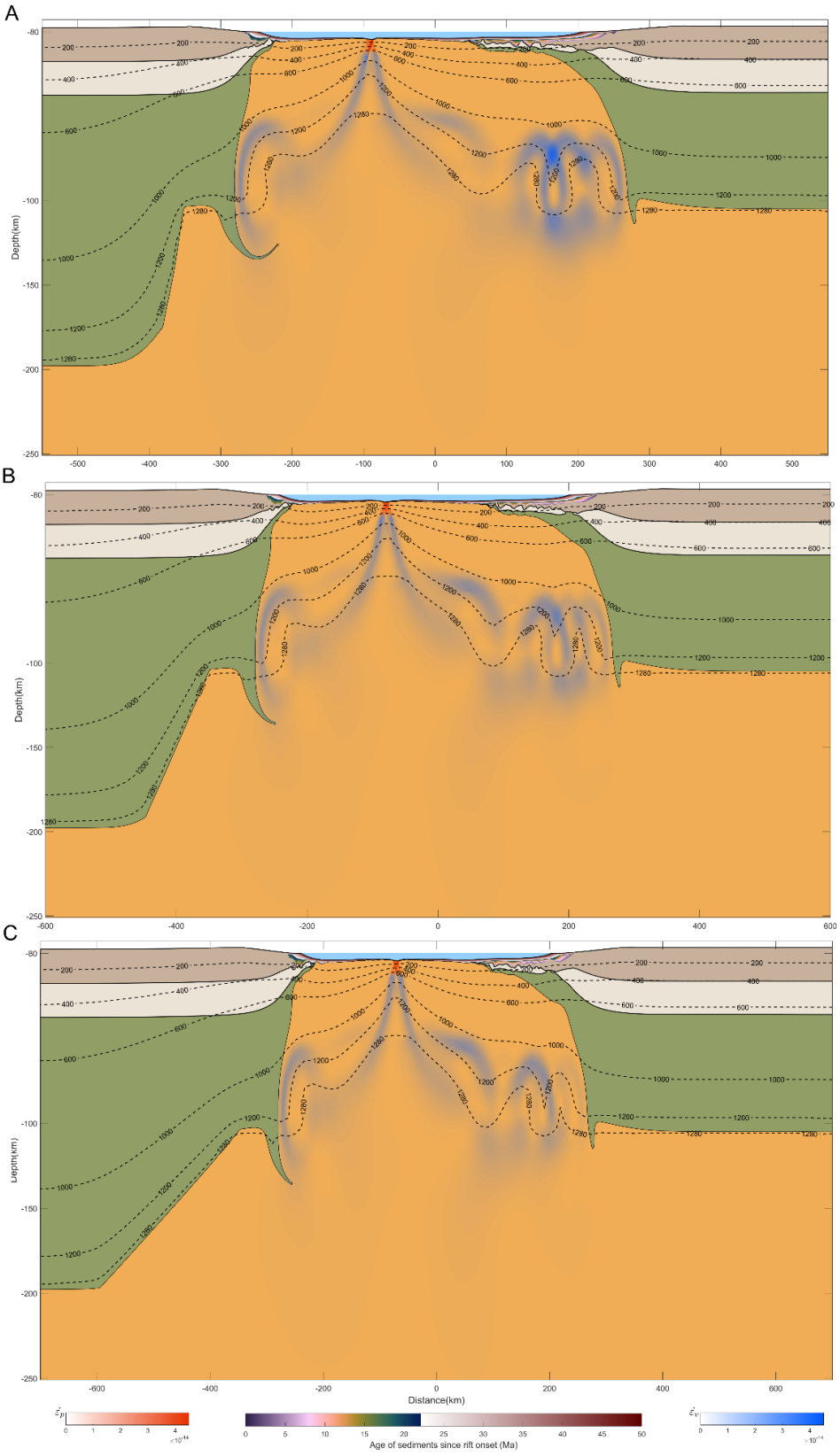

Figure S6 Snapshots of the craton models at 50 m.y. with initial crustal thickness of 40 km and thermal weak seed at 50 km from the craton edge with (A) initial slope of the LAB at the craton-mobile belt edge is 60^{o}, (B) initial slope of the LAB at the craton-mobile belt edge is 40^{o}, (C) initial slope of the LAB at the craton-mobile belt edge is 20^{o}. Plastic and viscous strain rates [s^{-1}] by red, blue shadings respectively and sediments color-coded by age are shown. The sea-level and water is represented by the cyan patch on the top. The color codings for layers is similar to that of Fig. S1. The isotherms are shown in black dashed lines with labels indicating the temperature [^{o}C] at the base of upper crust, lower crust and the LAB.

Figure S7: Craton Model with a weak seed of over-thickened crust

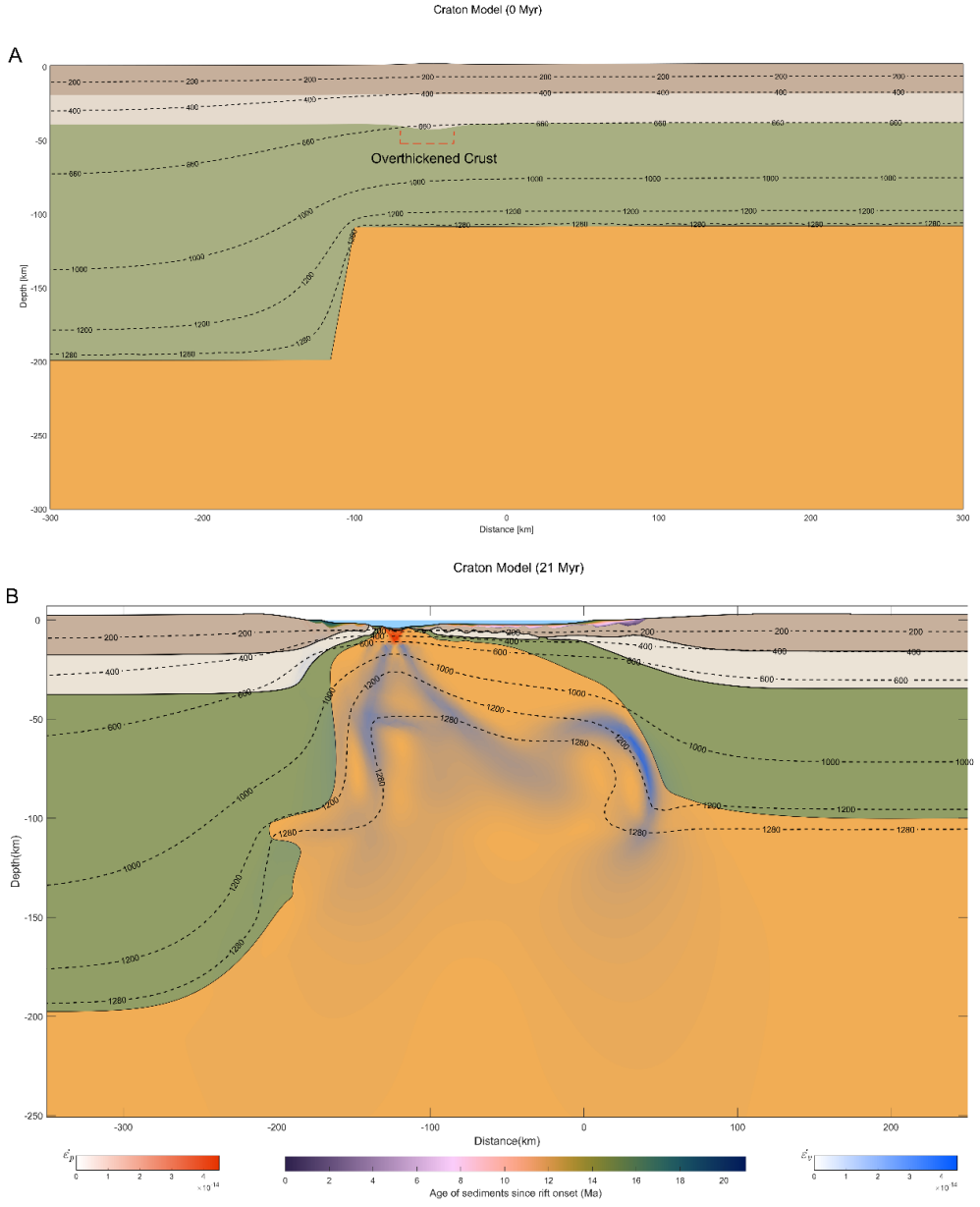

Figure S7 Snapshots of a craton model with 40 km initial crustal thickness with a weak seed consisting of over-thickened crust (20 km wide x 4 km thick) at a distance of 50 km from the craton mobile-belt edge at (A) model start (with overthickened crust weak seed as shown) and (B) at break-up time (21 m.y.). The isotherms indicating the temperature [^{o}C] are shown in black dashed lines. Plastic, viscous strain rates [s^{-1}] by red, blue shadings respectively and sediments color-coded by age are shown. The sea-level and water is represented by the cyan patch on the top.

Table S1. Model parameters and rheological constants used for numerical models

Thermomechanical parameters Variable [unit]	Wet Quarzite (UC)	Wet Anorthite (LC)	Dry Olivine (LM)	Wet Olivine (AM)
Dislocation pre-exponential factor log (B_{dis}) [Pa^{-n} s^{-1}]	-28.0	-15.4	-15.96	-15.81
Dislocation exponent n_{dis}	4.0	3.0	3.5	3.5
Dislocation activation energy E_{dis} [kJ/mol]	223	356	530	480
Dislocation activation volume V_{dis} [10^{-6} m^3/mol]	-	-	13	10
Diffusion pre-exponential factor log (B_{dif}) [Pa^{-n} s^{-1}]	-	-	-8.16	-8.64
Diffusion exponent n_{dif}	-	-	1	1
Diffusion activation energy E_{dif} [kJ/mol]	-	-	375	335
Diffusion activation volume V_{dif} [10^{-6} m^3/mol]	-	-	6	4
Shear Modulus μ [GPa]	36	40	74	74
Thermal conductivity k [Wm^{-1} K^{-1}]	2.5	2.5	3.3	3.3
Heat capacity C_P [J kg^{-1} K^{-1}]	1200	1200	1200	1200
Radiogenic heat production H_0 [μWm^{-3}]	1.1	0.13	0	0
Bulk Density ρ_0 [kg m^{-3}]	2700.	2850.	3360.	3360.
Thermal expansivity coefficient α [10^{-5} K^{-1}]	2.4	2.4	3.0	3.0
Cohesion (MPa)	10	10	10	10
Initial friction angle (degrees)	30	30	30	30
Final friction angle (degrees)	15	15	15	15
Constants	Value			
Triaxial scaling parameter F	$F = (2^{(1-n^{-1})}\ 3^{(0.5(1+n^{-1}))})^{-1}$			
Depletion factor for density dependence β[b]	0.04			
Surface process parameters				
Subaerial hillslope diffusion K [m^2/year][c]	0.25			
Subaerial discharge transport coefficient c [d]	10^{-3}			
Submarine diffusion coefficient K_s [m^2/year] [e]	10^3			
Submarine diffusion coefficient decay λ_s [m^{-1}] [f]	5 x 10^{-4}			
Pelagic sediment rate S [m/year] [g]	5 x 10^{-5}			
Pelagic sediment rate below CCD [m/year] [g]	10 x 10^{-5}			
Carbonate compensation depth (CCD) [m]	4000			
Precipitation rate δ [$m/year$] [h]	1			

Note: Diffusion creep B is calculated using a grain size of 6 mm. Wet olivine water content is 500 ppm H/Si. Rheological parameters for upper crust (UC), lower crust (LC), lithospheric mantle(LM), and asthenospheric mantle(AM) are from Gleason and Tullis (1995), Rybacki and Dresen

(2000) and Hirth and Kohlstedt (2003). [b]Depletion factor for density dependence β is from Schutt and Lesher (2006). Remaining parameters from Turcotte and Schubert (2002).[c]Subaerial hillslope diffusion K [d]Subaerial discharge transport coefficient are from Armitage et al. (2015). [g]Pelagic sedimentation rate is from Armitage et al. (2014), Marr et al. (2000), and Paola et al. (1992). [e]Submarine diffusion coefficient Ks, [f]Submarine diffusion coefficient decay are from Kaufman et al. (1991). [h]Precipitation rate α is from Huffman et al. (2009).

Supplementary Movie S1

Evolution of a craton model (40 km initial crustal thickness) with the initial weak seed at a distance of 50 km from the craton edge showing the flexural tectonic subsidence history of 3 markers chosen on the conjugate margins till 25 m.y. after rift initiation. The markers (circles on craton margin, triangles on mobile-belt margin) on either margin with same color are underlain by the same crustal thickness (Refer to Fig. 4B). (A) Model domain till 250 km depth. The upper and lower crust along with lithospheric and asthenospheric mantle are color coded as follows: Light brown: upper crust, beige: lower crust, green: lithospheric mantle, orange: asthenosphere.(Refer to Fig. S1). The red and blue shades indicate the areas of plastic and ductile strain rate [s^{-1}]. The sea-level and water is represented by the cyan patch on the top. The black dashed lines are isotherms with the temperature values [^{o}C] indicated along the lines. Sediments color-coded by age are also shown. (B) Model domain of the top 20 km showing the stratigraphic evolution of the rifted margins along with the markers shown in A. Note the craton model evolves into an asymmetric rifted architecture and results in the formation of narrow margin on the craton side and vice-versa. The wide hyper-extended mobile-belt margin experiences late synrift subsidence because of thermal relaxation and created favorable conditions for formation of late synrift, early postrift sag basins. (C) The tectonic subsidence of the markers chosen in (A and B) is plotted at each time step of the evolution denoting the subsidence of the location of the markers. Breakup occurs at 21 m.y. from the rift initiation and is indicated by red dashed vertical line. Deep rooted faults are active on the craton margin before breakup time (12-19 m.y.) leading to formation of thick sedimentary sequences derived from the erosion of the elevated craton rift shoulder. Strong

519 lateral and vertical thermal gradients are observed at the narrow craton margin as a result of
520 asymmetric asthenospheric uplift during the rift evolution.

521 **Supplementary Movie S2**

522 Evolution of a craton model (40 km initial crust thickness) with the initial weak seed at a
523 distance of 50 km from the craton edge during the postrift phase showing the flexural tectonic
524 subsidence history of 3 markers chosen on either conjugate till 121 m.y. (100 m.y. after break-up).
525 The circular markers are on the craton margin and the triangular markers are on the mobile-belt
526 margin. The markers on either margin with same color are underlain by the same crustal thickness
527 (Refer to Fig. 4B). A) Model domain till 250 km depth. The upper and lower crust along with
528 lithospheric and asthenospheric mantle are color coded as follows: Light brown: upper crust, beige:
529 lower crust, green: lithospheric mantle, orange: asthenosphere. The red and blue shades indicate
530 the areas of plastic and ductile strain rate [s^{-1}]. The sea-level and water is represented by the cyan
531 patch on the top. The black dashed lines are isotherms with the temperature values [^{o}C] indicated
532 along the lines. Sediments color-coded by age are also shown. (B) Model domain till 100 km depth
533 showing the craton margin with the markers (circles) as shown in (A) to the left and mobile-belt
534 margin showing the markers (triangles) as shown in (A) to the right. C) The tectonic subsidence
535 of the markers chosen in (A and B) is plotted at each time step of the evolution denoting the
536 subsidence of the location of the markers. Breakup occurs at 21 m.y. from the rift initiation and is
537 indicated by red dashed vertical line. Notice that the difference in the tectonic subsidence of the
538 corresponding markers denoted by the same color varies by ~1000 m at 100 m.y. post breakup.

539

540

541

References:

Afonso, J. C., Ben-Mansour, W., O'Reilly, S. Y., Griffin, W. L., Salajegheh, F., Foley, S., Begg, G., Selway, K., Macdonald, A., and Januszczak, N., 2022, Thermochemical structure and evolution of cratonic lithosphere in central and southern Africa: Nature Geoscience, v. 15, no. 5, p. 405-410.

Alkmim, F. F., and Martins-Neto, M. A., 2012, Proterozoic first-order sedimentary sequences of the São Francisco craton, eastern Brazil: Marine and Petroleum Geology, v. 33, no. 1, p. 127-139.

Andrés-Martínez, M., Morgan, J. P., Pérez-Gussinyé, M., and Rüpke, L., 2015, A new free-surface stabilization algorithm for geodynamical modelling: Theory and numerical tests: Physics of the Earth and Planetary Interiors, v. 246, p. 41-51.

Andrés-Martínez, M., Pérez-Gussinyé, M., Armitage, J., and Morgan, J. P., 2019, Thermomechanical implications of sediment transport for the architecture and evolution of continental rifts and margins: Tectonics, v. 38, no. 2, p. 641-665.

Armitage, J., Duller, R., and Schmalholz, S., 2014, The influence of long-wavelength tilting and climatic change on sediment accumulation: Lithosphere, v. 6, no. 5, p. 303-318.

Armitage, J. J., Allen, P. A., Burgess, P. M., Hampson, G. J., Whittaker, A. C., Duller, R. A., and Michael, N. A., 2015, Sediment Transport Model For the Eocene Escanilla Sediment-Routing System: Implications For the Uniqueness of Sequence Stratigraphic ArchitecturesSEDIMENT TRANSPORT MODEL FOR THE EOCENE ESCANILLA: Journal of Sedimentary Research, v. 85, no. 12, p. 1510-1524.

Aslanian, D., and Moulin, M., 2013, Palaeogeographic consequences of conservational models in the South Atlantic Ocean: Geological Society, London, Special Publications, v. 369, no. 1, p. 75-90.

Begg, G., Griffin, W., Natapov, L., O'Reilly, S. Y., Grand, S., O'Neill, C., Hronsky, J., Djomani, Y. P., Swain, C., and Deen, T., 2009, The lithospheric architecture of Africa: Seismic tomography, mantle petrology, and tectonic evolutionThe lithospheric architecture of Africa: Geosphere, v. 5, no. 1, p. 23-50.

Brodie, K., and Rutter, E., 1987, The role of transiently fine-grained reaction products in syntectonic metamorphism: natural and experimental examples: Canadian Journal of Earth Sciences, v. 24, no. 3, p. 556-564.

Burov, E. B., and Diament, M., 1995, The effective elastic thickness (T e) of continental lithosphere: What does it really mean?: Journal of Geophysical Research: Solid Earth, v. 100, no. B3, p. 3905-3927.

Cavalcante, C., Fossen, H., de Almeida, R. P., Hollanda, M. H. B., and Egydio-Silva, M., 2019, Reviewing the puzzling intracontinental termination of the Araçuaí-West Congo orogenic belt and its implications for orogenic development: Precambrian Research, v. 322, p. 85-98.

Celli, N. L., Lebedev, S., Schaeffer, A. J., and Gaina, C., 2020, African cratonic lithosphere carved by mantle plumes: Nature communications, v. 11, no. 1, p. 92.

Ciardelli, C., Assumpção, M., Bozdağ, E., and van der Lee, S., 2022, Adjoint waveform tomography of South America: Journal of Geophysical Research: Solid Earth, v. 127, no. 2, p. e2021JB022575.

Cunha, T., 2008, Gravity anomalies, flexure and the thermo-mechanical evolution of the West Iberia Margin and its conjugate of Newfoundland [Ph.D. thesis]: University of Oxford.

587 Dabrowski, M., Krotkiewski, M., and Schmid, D., 2008, MILAMIN: MATLAB-based finite
588 element method solver for large problems: Geochemistry, Geophysics, Geosystems, v. 9,
589 no. 4.
590 Davison, I., 1997, Wide and narrow margins of the Brazilian South Atlantic: Journal of the
591 Geological Society, v. 154, no. 3, p. 471-476.
592 Delph, J. R., and Porter, R. C., 2015, Crustal structure beneath southern Africa: insight into how
593 tectonic events affect the Mohorovičić discontinuity: Geophysical Journal International, v.
594 200, no. 1, p. 254-264.
595 Doin, M. P., Fleitout, L., and Christensen, U., 1997, Mantle convection and stability of depleted
596 and undepleted continental lithosphere: Journal of Geophysical Research: Solid Earth, v.
597 102, no. B2, p. 2771-2787.
598 Durrheim, R. J., and Mooney, W. D., 1994, Evolution of the Precambrian lithosphere:
599 seismological and geochemical constraints: Journal of Geophysical Research: Solid Earth,
600 v. 99, no. B8, p. 15359-15374.
601 Eagles, G., 2007, New angles on South Atlantic opening: Geophysical Journal International, v.
602 168, no. 1, p. 353-361.
603 Feng, M., Van der Lee, S., and Assumpção, M., 2007, Upper mantle structure of South America
604 from joint inversion of waveforms and fundamental mode group velocities of Rayleigh
605 waves: Journal of Geophysical Research: Solid Earth, v. 112, no. B4.
606 Ford, H. A., Fischer, K. M., Abt, D. L., Rychert, C. A., and Elkins-Tanton, L. T., 2010, The
607 lithosphere–asthenosphere boundary and cratonic lithospheric layering beneath Australia
608 from Sp wave imaging: Earth and Planetary Science Letters, v. 300, no. 3-4, p. 299-310.
609 Fullea, J., Muller, M., and Jones, A., 2011, Electrical conductivity of continental lithospheric
610 mantle from integrated geophysical and petrological modeling: Application to the
611 Kaapvaal Craton and Rehoboth Terrane, southern Africa: Journal of Geophysical
612 Research: Solid Earth, v. 116, no. B10.
613 Gleason, G. C., and Tullis, J., 1995, A flow law for dislocation creep of quartz aggregates
614 determined with the molten salt cell: Tectonophysics, v. 247, no. 1-4, p. 1-23.
615 Handy, M. R., Hirth, G., and Hovius, N., 2007, Continental fault structure and rheology from the
616 frictional-to-viscous transition downward.
617 Heine, C., Zoethout, J., and Müller, R. D., 2013, Kinematics of the South Atlantic rift: Solid Earth,
618 v. 4, no. 2, p. 215-253.
619 Hirth, G., and Kohlstedf, D., 2003, Rheology of the upper mantle and the mantle wedge: A view
620 from the experimentalists: Geophysical monograph-american geophysical union, v. 138, p.
621 83-106.
622 Huffman, G. J., Adler, R. F., Bolvin, D. T., and Gu, G., 2009, Improving the global precipitation
623 record: GPCP version 2.1: Geophysical Research Letters, v. 36, no. 17.
624 Kaufman, P., Grotzinger, J., McCormick, D., Franseen, E., and Watney, W., 1991, Depth-
625 dependent diffusion algorithm for simulation of sedimentation in shallow marine
626 depositional systems: Kansas Geological Survey Bulletin, v. 233, p. 489-508.
627 Kgaswane, E. M., Nyblade, A. A., Julia, J., Dirks, P. H., Durrheim, R. J., and Pasyanos, M. E.,
628 2009, Shear wave velocity structure of the lower crust in southern Africa: Evidence for
629 compositional heterogeneity within Archaean and Proterozoic terrains: Journal of
630 Geophysical Research: solid earth, v. 114, no. B12.
631 Khoza, T. D., Jones, A. G., Muller, M. R., Evans, R. L., Miensopust, M. P., and Webb, S. J., 2013,
632 Lithospheric structure of an Archean craton and adjacent mobile belt revealed from 2-D

633 and 3-D inversion of magnetotelluric data: Example from southern Congo craton in
634 northern Namibia: Journal of Geophysical Research: Solid Earth, v. 118, no. 8, p. 4378-
635 4397.
636 Lenardic, A., and Moresi, L. N., 1999, Some thoughts on the stability of cratonic lithosphere:
637 Effects of buoyancy and viscosity: Journal of Geophysical Research: Solid Earth, v. 104,
638 no. B6, p. 12747-12758.
639 Marr, J., Swenson, J. B., Paola, C., and Voller, V. R., 2000, A two-diffusion model of fluvial
640 stratigraphy in closed depositional basins: Basin Research, v. 12, no. 3-4, p. 381-398.
641 Meisling, K. E., Cobbold, P. R., and Mount, V. S., 2001, Segmentation of an obliquely rifted
642 margin, Campos and Santos basins, southeastern Brazil: AAPG bulletin, v. 85, no. 11, p.
643 1903-1924.
644 Moresi, L., Dufour, F., and Mühlhaus, H.-B., 2003, A Lagrangian integration point finite element
645 method for large deformation modeling of viscoelastic geomaterials: Journal of
646 computational physics, v. 184, no. 2, p. 476-497.
647 Morgan, J. P., 1997, The generation of a compositional lithosphere by mid-ocean ridge melting
648 and its effect on subsequent off-axis hotspot upwelling and melting: Earth and Planetary
649 Science Letters, v. 146, no. 1-2, p. 213-232.
650 Morgan, J. P., and Chen, Y. J., 1993, The genesis of oceanic crust: Magma injection, hydrothermal
651 circulation, and crustal flow: Journal of Geophysical Research: Solid Earth, v. 98, no. B4,
652 p. 6283-6297.
653 Naliboff, J., and Buiter, S. J., 2015, Rift reactivation and migration during multiphase extension:
654 Earth and Planetary Science Letters, v. 421, p. 58-67.
655 Paola, C., Heller, P. L., and Angevine, C. L., 1992, The large-scale dynamics of grain-size
656 variation in alluvial basins, 1: Theory: Basin research, v. 4, no. 2, p. 73-90.
657 Pérez-Díaz, L., and Eagles, G., 2014, Constraining South Atlantic growth with seafloor spreading
658 data: Tectonics, v. 33, no. 9, p. 1848-1873.
659 Pérez-Gussinyé, M., Andrés-Martínez, M., Araújo, M., Xin, Y., Armitage, J., and Morgan, J.,
660 2020, Lithospheric strength and rift migration controls on synrift stratigraphy and breakup
661 unconformities at rifted margins: Examples from numerical models, the Atlantic and South
662 China Sea Margins: Tectonics, v. 39, no. 12, p. e2020TC006255.
663 Phipps Morgan, J., 2001, Thermodynamics of pressure release melting of a veined plum pudding
664 mantle: Geochemistry, Geophysics, Geosystems, v. 2, no. 4.
665 Platt, J., and Behr, W., 2011, Grainsize evolution in ductile shear zones: Implications for strain
666 localization and the strength of the lithosphere: Journal of Structural Geology, v. 33, no. 4,
667 p. 537-550.
668 Précigout, J., and Gueydan, F., 2009, Mantle weakening and strain localization: Implications for
669 the long-term strength of the continental lithosphere: Geology, v. 37, no. 2, p. 147-150.
670 Ranalli, G., 1995, Rheology of the Earth, Springer Science & Business Media.
671 Ranero, C. R., and Pérez-Gussinyé, M., 2010, Sequential faulting explains the asymmetry and
672 extension discrepancy of conjugate margins: Nature, v. 468, no. 7321, p. 294-299.
673 Regenauer-Lieb, K., Weinberg, R. F., and Rosenbaum, G., 2006, The effect of energy feedbacks
674 on continental strength: Nature, v. 442, no. 7098, p. 67-70.
675 Ritsema, J., and van Heijst, H., 2000, New seismic model of the upper mantle beneath Africa:
676 Geology, v. 28, no. 1, p. 63-66.
677 Ros, E., Pérez-Gussinyé, M., Araújo, M., Thoaldo Romeiro, M., Andrés-Martínez, M., and
678 Morgan, J. P., 2017, Lower crustal strength controls on melting and serpentinization at

magma-poor margins: Potential implications for the South Atlantic: Geochemistry, Geophysics, Geosystems, v. 18, no. 12, p. 4538-4557.
Rybacki, E., and Dresen, G., 2000, Dislocation and diffusion creep of synthetic anorthite aggregates: Journal of Geophysical Research: Solid Earth, v. 105, no. B11, p. 26017-26036.
Salazar-Mora, C. A., and Sacek, V., 2021, Lateral flow of thick continental lithospheric mantle during tectonic quiescence: Journal of Geodynamics, v. 145, p. 101830.
Schutt, D., and Lesher, C., 2006, Effects of melt depletion on the density and seismic velocity of garnet and spinel lherzolite: Journal of Geophysical Research: Solid Earth, v. 111, no. B5.
Tommasi, A., Mainprice, D., Canova, G., and Chastel, Y., 2000, Viscoplastic self-consistent and equilibrium-based modeling of olivine lattice preferred orientations: Implications for the upper mantle seismic anisotropy: Journal of Geophysical Research: Solid Earth, v. 105, no. B4, p. 7893-7908.
Trompette, R., and Carozzi, A., 1994, Pan-African Brasiliano Aggregation of South America and Africa: Geology of Gondwana (2000-500 Ma), Rotterdam, Balkema, p. 350.
Turcotte, D. L., and Schubert, G., 2002, Geodynamics, Cambridge university press.
Van Schmus, W., Oliveira, E., Da Silva Filho, A., Toteu, S., Penaye, J., and Guimarães, I., 2008, Proterozoic links between the Borborema province, NE Brazil, and the central African fold belt: Geological Society, London, Special Publications, v. 294, no. 1, p. 69-99.